

# Microstructure of Equal-Channel Angular Pressed Cu and Cu-Zr Samples Studied by Different Methods

R. KUŽEL, M. JANEČEK, Z. MATĚJ, J. ČÍŽEK, M. DOPITA, and O. SRBA

Polycrystalline samples of technical-purity Cu (99.95 wt pct) and Cu with 0.18 wt pct Zr have been processed at room temperature by equal-channel angular pressing (ECAP). The microstructure evolution and its fragmentation after ECAP were investigated by transmission electron microscopy (TEM), electron backscattered diffraction (EBSD), positron annihilation spectroscopy (PAS), and by X-ray diffraction (XRD) line-profile analysis. The first two techniques revealed an increase in the fraction of high-angle grain boundaries (HAGBs), with increasing strain reaching the value of 90 pct after eight ECAP passes. The increase was more pronounced for pure Cu samples. The following two kinds of defects were identified in ECAP specimens by PAS: (1) dislocations that represent the dominant kind of defects and (2) small vacancy clusters (so-called microvoids). A detailed XRD line-profile analysis was performed by the analysis of individual peaks and by total profile fitting. A slight increase in the dislocation density with the number of ECAP passes agreed with the PAS results. Variations in microstructural features obtained by TEM and EBSD can be related to the changes in the XRD line-broadening anisotropy and dislocation-correlation parameter.

DOI: 10.1007/s11661-009-9895-0

© The Minerals, Metals & Materials Society and ASM International 2009

## I. INTRODUCTION

RESEARCH activity in the area of severe plastic deformation (SPD) has increased tremendously in the last years because of the many interesting properties that can be achieved in bulk materials by SPD.<sup>[1]</sup> Compared to classical deformation processes, the main advantage of SPD techniques is the lack of shape-change deformation and the consequent possibility for imparting extremely large strain. The techniques of SPD have received enormous interest over the last two decades as methods capable of producing fully dense and bulk submicrocrystalline and nanocrystalline materials. Significant grain refinement obtained by SPD leads to improvements in mechanical, microstructural, and physical properties.<sup>[2]</sup> Recent investigations of ultrafine-grained (UFG) materials have concentrated mainly on structural characterization,<sup>[3–5]</sup> microhardness variation,<sup>[6,7]</sup> mechanical properties,<sup>[8,9]</sup> elastic and damping properties,<sup>[10]</sup> fatigue,<sup>[11]</sup> and creep.<sup>[12]</sup> Several models

have been also developed to relate the mechanical properties of the UFG metals to the evolution of the microstructure and texture.<sup>[13–15]</sup>

Equal-channel angular pressing (ECAP) has been identified as an efficient method for obtaining submicrocrystalline (grain size  $d < 1 \mu\text{m}$ ) or nanocrystalline ( $d < 100 \text{ nm}$ ) grain sizes in bulk metallic materials. The ECAP technique allows the repetitive pressing of a billet through a die that has two intersecting channels without changing its cross-sectional dimensions. Very high shear strains can therefore be produced.

Copper represents an ideal model material for studying the processes of deformation and microstructure evolution, due to its low-cost, simple fcc structure, medium stacking-fault energy (SFE), and the long history of research of this material prepared by conventional techniques such as, for example, rolling, extrusion, compression, wire drawing, *etc.*, that were capable of imparting large strains to the workpiece. This investigation represents the basis of our knowledge and understanding of the properties and the associated microstructure changes in SPD copper.<sup>[16]</sup>

Numerous experimental data reporting various properties of UFG Cu prepared by SPD are now available (*e.g.*, Reference 17), providing excellent reviews and many references from the literature. It was found that, with an increasing number of passes, the microstructure changes from a strongly elongated shear-band structure toward a more equiaxed subgrain and grain structure. This is accompanied by a decrease in the cell wall boundary width and an increase in the recovered or recrystallized grain structure. The fine microstructure of pure copper is very unstable. Recovery and recrystallization can occur at rather low temperatures. Therefore, composites and alloys are prepared. The impurities or

---

R. KUŽEL, Associate Professor and Head of Department, and Z. MATĚJ, Postdoctoral Student, Department of Condensed Matter Physics, M. JANEČEK, Associate Professor and Head of Department, and O. SRBA, Postdoctoral Student, Department of Physics of Materials, and J. ČÍŽEK, Senior Assistant Professor, Department of Low Temperature Physics, are with the Faculty of Mathematics and Physics, Charles University in Prague, 121 16 Prague 2, Czech Republic. Contact e-mail: kuzel@karlov.mff.cuni.cz M. DOPITA, Postdoctoral Student, is with the Institute of Materials Science, TU Bergakademie Freiberg, D-09599 Freiberg, Germany.

This article is based on a presentation given in the symposium entitled “Neutron and X-Ray Studies of Advanced Materials” which occurred February 15–19, 2009 during the TMS Annual Meeting in San Francisco, CA, under the auspices of TMS, TMS Structural Materials Division, TMS/ASM Mechanical Behavior of Materials Committee, TMS: Advanced Characterization, Testing, and Simulation Committee, and TMS: Titanium Committee.

Article published online June 26, 2009

precipitates can stabilize the UFG microstructure to a much higher temperature. Copper with different amounts of  $\text{Al}_2\text{O}_3$  was studied, for example, in Reference 18. In this article, in addition to pure Cu samples, samples of the binary CuZr alloy were investigated.

The dependence of the microstructure of the samples on the number of passes ( $N = 1, 2, 4,$  and  $8$ ) was investigated by transmission electron microscopy (TEM) and electron backscattered diffraction (EBSD). The latter technique, due to the combination of its good spatial and angular resolution, yields unique information about the local preferred orientation of crystallites, the grain/subgrain morphology and size distributions, the grain-boundary (GB) misorientations, and the character distributions, type, and frequencies of the GBs, and the deformation state of the specimens.

The absence of the signal from free positrons in the positron annihilation spectroscopy (PAS) spectra revealed the presence of a high density of lattice defects, in particular dislocations and microvoids.

The specimens well characterized by these techniques were also studied by X-ray diffraction (XRD) line-profile analysis, with the aim of finding out how the observed microstructural differences are reflected in XRD patterns and, consequently, what type of information XRD can provide about the microstructural features of UFG material.

## II. EXPERIMENTAL PROCEDURES

### A. Sample Preparation

Technical-purity (99.95 pct) Cu and Cu with an addition of 0.18 wt pct of Zr were severely deformed by ECAP to a maximum equivalent strain of eight ( $N = 1, 2, 4,$  and  $8$  passes) at room temperature following route  $B_c$ . Prior to ECAP processing, the specimens were annealed for 2 hours at  $450^\circ\text{C}$  in a protective inert atmosphere. The initial specimen dimensions were  $10 \times 10 \times 60$  mm. The ECAP was carried out using a split-design die manufactured from tool steel X38CrMoV51. The details of the die design as well as the ECAP are given elsewhere.<sup>[19]</sup>

### B. Experimental Techniques

For the TEM investigations on specimens prepared by mechanical and electrolytic polishing from the middle sections of the ECAP-processed billets in the plane perpendicular to the extrusion direction of the billet (plane  $X^{[1]}$ ), a JEOL\* 2000FX electron

---

\*JEOL is a trademark of Japan Electron Optics Ltd., Tokyo.

microscope operating at 200 kV was used. Electrolytic polishing was carried out at  $10^\circ\text{C}$  using 50 pct  $\text{H}_3\text{PO}_4$  in a Tenupol 5 jet-polishing unit (Struers\*\*).

---

\*\*Struers is a trademark of Struers A/S, Ballerup, Denmark.

The EBSD investigations were performed on sections taken from plane  $X$  of the ECAP specimens. Because the EBSD measurement is extremely surface sensitive (measured information comes from the depth of several tenths of nanometers of the specimen), it is necessary to prepare the sample surface properly. In particular, the sample regions strained and disturbed by the specimen cutting have to be removed. The polishing procedure was completed using the following steps. To start with, the specimens were mechanically grinded using silicon carbide grinding plates with decreasing roughness; they were then polished with 6-, 3-, and  $1\text{-}\mu\text{m}$  diamond paste; finally, the specimens were etched using  $0.04\text{-}\mu\text{m}$  colloidal silica.

The EBSD measurements were performed using the high-resolution scanning electron microscope LEO-1530 (Carl Zeiss<sup>†</sup>) equipped with a field-emission cathode and

---

<sup>†</sup>Carl Zeiss is a trademark of Carl Zeiss Semiconductor technologies A.G., Jena, Germany.

---

a Nordlys II EBSD detector (HKL Oxford Instruments<sup>‡</sup>).

---

<sup>‡</sup>HKL Oxford Instruments is a trademark of Oxford Instruments Nanoanalysis, Bucks, UK.

The measurements were carried out at an acceleration voltage of 20 kV, a working distance of 15 mm, and a sample tilt of  $70^\circ$ . The step size was varied from 50 to 500 nm, depending on the grain size (*i.e.*, the number of ECAP cycles). For identification and indexing of the Kikuchi patterns and measured data evaluation, the software package Channel 5 (HKL Oxford Instruments<sup>§</sup>) was employed. The emphasis

---

<sup>§</sup>HKL Oxford Instruments is a trademark of Oxford Instruments Nanoanalysis, Bucks, UK.

during the EBSD investigation was put on the measurement of the center of the specimen, to avoid the measurement of the inhomogeneous parts of the samples that could occur on the rim of the samples. The scanning was performed in the transversal plane perpendicular to the direction of the ECAP (plane  $X$ ).

The PAS method is a well-established method with a high sensitivity to open-volume defects such as vacancies, dislocations, misfit defects, *etc.*<sup>[20]</sup> In this work, we employed positron lifetime (PL) spectroscopy, which enabled the identification of open-volume defects and the determination of defect densities in the specimens studied. A  $^{22}\text{Na}_2\text{CO}_3$  positron source ( $\sim 1.5$  MBq) deposited on a  $2\text{-}\mu\text{m}$ -thick Mylar foil was used in this work. The positron source was always forming a sandwich with two identical specimens. A fast-fast PL spectrometer<sup>[21]</sup> with an excellent time resolution of 160 ps (full-width at half-maximum  $^{22}\text{Na}$ ) was used for the PL studies. At least  $10^7$  positron annihilation events were accumulated at each PL spectrum, which was subsequently decomposed using a maximum likelihood procedure.<sup>[22]</sup>

Measurements done with XRD were carried out with the aid of an X'Pert Pro powder diffractometer (PANalytical B.V., Almelo, The Netherlands), filtered Cu K $\alpha$  radiation, a variable divergence, and antiscatter slits enhancing high-angle peaks important for the line-profile analysis and the PIXCel position-sensitive detector (PANalytical B.V., Almelo, The Netherlands) in obtaining high-quality low-noise data in a reasonable collection time. Line-profile analysis was done using the following three methods: (1) the simplified integral breadth method, (2) the analysis of the half-width and integral breadth of individual profiles through the fitting of the convolution of instrumental and physical functions, the latter based on the dislocation model, and (3) the total-pattern fitting by the FOX program (Vincent Favre-Nicolin, Geneva, Switzerland, <http://vincefn.net/Fox/>) that was modified for analysis of the crystallite size and strain, including dislocation-induced line broadening.<sup>[23]</sup> Texture measurements were performed with a PHILIPS<sup>®</sup> X'Pert MRD Pro system equipped

with a Eulerian cradle and polycapillary in the primary beam. A step size of 3 deg for both angles and a time of 20 s/step were selected.

Mechanical properties were determined by tensile tests in a conventional universal screw-driven Instron 5882 machine (Instron<sup>®</sup>) at the initial strain rate of

<sup>®</sup>Instron is a trademark of Instron Ltd., High Wycombe, UK.

$4 \times 10^{-4} \text{ s}^{-1}$  at room temperature.

### III. RESULTS AND DISCUSSION

#### A. Mechanical Properties

The true-stress–true-strain curves for the initial coarse-grained (CG) material and the specimens after ECAP ( $N = 1, 2, 4,$  and  $8\text{P}$ ) are shown in Figure 1(a). Table I and II shows a quantitative summary of the tensile test data after 0, 1, 2, 4, and 8 passes represented in terms of the yield stress (YS) ( $\sigma_{0.2}$ ), the ultimate tensile strength (UTS) ( $\sigma_{\text{max}}$ ), and the total

<sup>®</sup>PHILIPS is a trademark of Philips Electronic Instruments Corp., Mahwah, NJ.

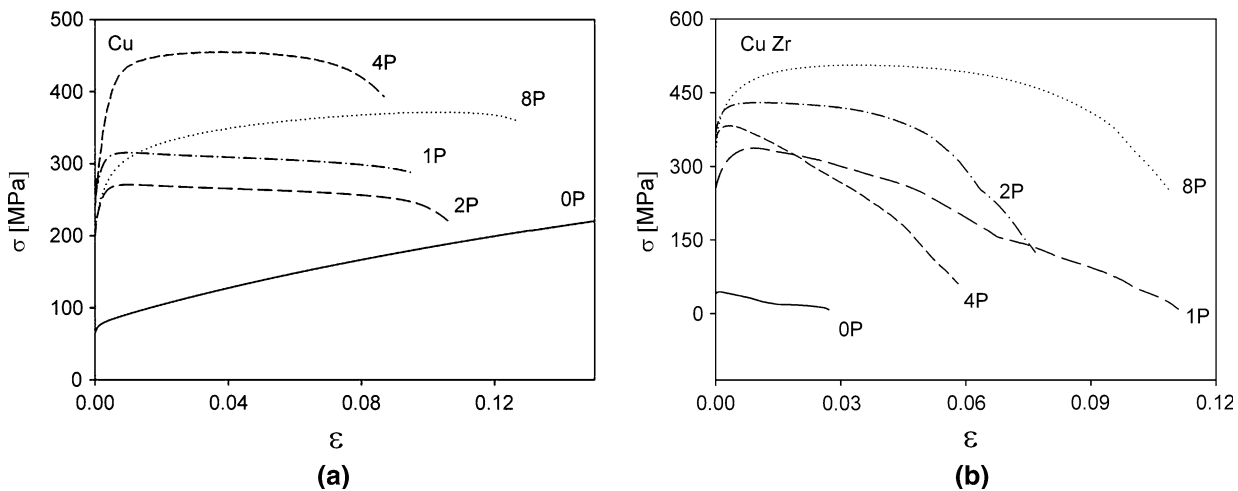


Fig. 1—Stress-strain curves of (a) Cu and (b) Cu Zr.

**Table I. Summary of Experimental Data Obtained from Mechanical Testing of Cu Specimens**

Number of Passes ( $N$ )	0	1	2	4	8
$\sigma_{0.2}$ (MPa)	$78 \pm 5$	$293 \pm 20$	$250 \pm 20$	$303 \pm 18$	$258 \pm 15$
$\sigma_{\text{max}}$ (MPa)	$215 \pm 12$	$314 \pm 15$	$270 \pm 20$	$455 \pm 22$	$371 \pm 20$
$\epsilon_{\text{tot}}$ (pct)	$40 \pm 2$	$9,5 \pm 0,5$	$10,6 \pm 0,4$	$8,7 \pm 0,5$	$12,7 \pm 0,6$

**Table II. Summary of Experimental Data Obtained from Mechanical Testing of CuZr Specimens**

Number of Passes ( $N$ )	0	1	2	4	8
$\sigma_{0.2}$ (MPa)	43	$302 \pm 21$	$413 \pm 24$	$380 \pm 22$	$416 \pm 14$
$\sigma_{\text{max}}$ (MPa)	44	$336 \pm 19$	$429 \pm 17$	$382 \pm 24$	$506 \pm 23$
$\epsilon_{\text{tot}}$ (pct)	2,7	$11 \pm 0,5$	$7,6 \pm 0,9$	$5,8 \pm 0,8$	$10,8 \pm 0,7$

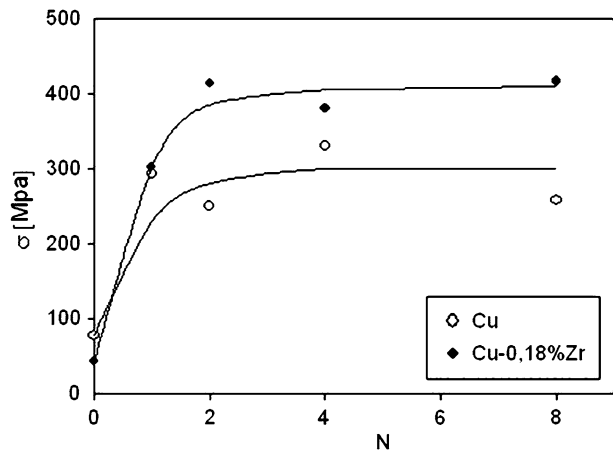


Fig. 2—Comparison of the YS in pure Cu and the CuZr alloy.

elongation ( $\epsilon_{\text{tot}}$ ). The Cu specimens subjected to ECAP show a significantly higher YS as compared to the CG specimen.

Both the YS and the UTS increase up to  $N = 4$  followed by a slight decline in the specimen  $N = 8$ . A significantly reduced total elongation ( $\epsilon_{\text{tot}} < 10$  pct) as compared to the CG Cu was observed for all passes. A slightly larger elongation ( $\epsilon_{\text{tot}} \approx 13$  pct) was found only in the 8P specimen. The measured values are in good agreement with the data reported by other authors on UFG Cu.<sup>[18]</sup> These authors also observed the increase in both the YS and UTS up to  $N = 4$  followed by a moderate decrease in both characteristic stresses in Cu samples deformed *via* route  $B_c$ . Similar observations were reported on Cu deformed by route C.<sup>[24]</sup> In general, all mechanical tests on specimens up to  $N = 8$  indicate limited ductility with total elongation values not exceeding 10 pct. A slightly larger uniform strain has been recently reported for specimens deformed for a higher number of passes ( $N > 16$ ) using route  $B_c$ .<sup>[25]</sup>

All values in Table I indicate an average value of two or three tests performed on specimens taken from different billets that underwent the same member of ECAP passes. The scatter of measured data did not usually exceed 5 to 6 pct of the respective measured value. Similar behavior was found in the binary alloy Cu0.18 wt pct Zr (Figure 1(b)). In this case, an almost monotonous increase in both characteristic stresses with an increasing number of passes was found. The fine-grained CuZr specimens exhibit very limited ductility, which did not exceed 12 pct, similar to pure copper.

In Figure 2, the comparison of the variation in YS as a function of strain due to the ECAP of both materials is presented. Systematically higher values of the YS were found in the alloy in the whole range of stresses. After a sharp increase in the YS in the specimen  $N = 1$ , the values tend to saturate after  $N = 2$ . An almost constant difference of approximately 120 MPa between the YS in the alloy and the pure Cu was found starting from the  $N = 2$  specimen.

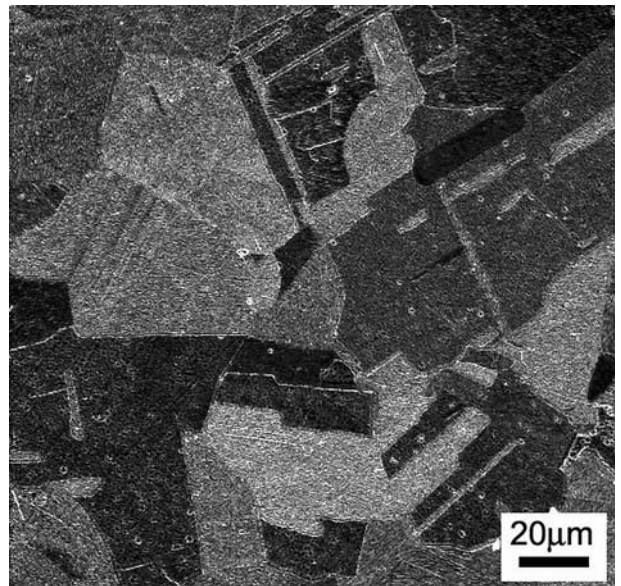


Fig. 3—Microstructure of the initial state of Cu.

## B. Transmission Electron Microscopy

### 1. Microstructural evolution in Cu

The SEM micrograph of the initial state before ECAP is shown in Figure 3. The microstructure consists of fully recrystallized grains. The extensive twinning associated with annealing at 450 °C is also seen. The average grain size, excluding twins, is approximately 30  $\mu\text{m}$ . Bright-field TEM micrographs showing the development of the microstructure oriented along the  $\langle 011 \rangle$  zone axis are presented in Figure 4. After one pass (Figure 4(a)), the microstructure mainly consists of strongly elongated dislocation cells or subgrains with an average cross-sectional size of 300 to 400 nm. Two types of boundaries can be recognized in this micrograph. The thick dark lines can be identified as lamellae boundaries<sup>[5]</sup> or dense dislocation walls (DDWs),<sup>[26]</sup> while the lighter and wider ones are individual dislocation cell boundaries. The DDWs usually enclose several cells and are classified as geometrically necessary boundaries, because they are necessary for the accommodation of lattice rotations in the adjoining volume. Selected area diffraction observations showed that these boundaries are mainly low-angle ones and are oriented along the trace of a  $\{111\}$  plane, which indicates that they are parallel to a  $\langle 110 \rangle$  shear direction. They are in a nonequilibrium state, because they contain a high density of extrinsic dislocations. In some regions (approximately 20 pct of the area investigated), a tangled dislocation structure typical of heavily deformed material was observed.

After the second pass (Figure 4(b)), the microstructure did not change significantly. Bands of elongated subgrains were found in all areas of the specimen. The average size of the individual boundaries slightly decreased to 200 to 300 nm. Most of the boundaries were still aligned along the trace of a  $\{111\}$  plane. In a few areas, lamellae boundaries oriented along a  $\{220\}$

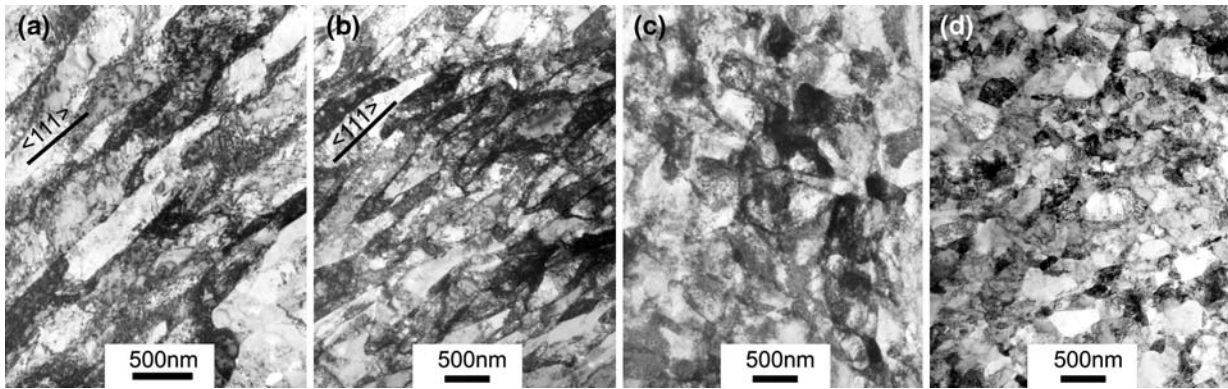


Fig. 4—Microstructure development during ECAP in Cu specimens:  $N = (a) 1, (b) 2, (c) 4, \text{ and } (d) 8$ .

plane trace were also observed. More equiaxed subgrains with a higher misorientation, indicating the activity of additional slip systems during the second pass, were also found locally.

After four passes (Figure 4(c)), the fraction of equiaxed subgrains increased and the larger proportion of high-angle grain boundaries (HAGBs) was observed in the structure. An equiaxed grain structure was found in approximately 40 to 50 pct of the observed area. This is an indication that many new slip systems not parallel to the original slip system became active between the second and fourth pass of pressing, reducing the length of the original subgrain boundaries.

Our observations are in good agreement with the comprehensive investigation of Agnew<sup>[11]</sup> and Mishin,<sup>[4,27]</sup> who reported a grain size of 300 nm in ECAP-deformed Cu. Moreover, these authors recognized that Cu subjected to ECAP exhibits elongated subgrain structures that are subdivided transversely by low-angle boundaries similar to those observed in coldrolled deformed structures;<sup>[26]</sup> this corresponds well with what we observed in the specimen after one pass of ECAP.

The microstructure of the specimen after eight passes is presented in Figure 4(d). It shows an almost homogeneous microstructure with equiaxed subgrains separated largely by HAGBs. The individual boundaries are straight, with sharp contrast and very few dislocations in the grain interior; they are obviously closer to the equilibrium state than the GBs in the specimens that underwent fewer ECAP passes. The average grain size ranged between 200 and 300 nm. In some areas, larger grains having the average size of approximately 500 nm were also found.

## 2. Microstructural evolution in Cu-0.18 pct Zr alloy

Light microscopy investigations indicate that the initial microstructure of the alloy CuZr consists of coarse recrystallized grains with an average size of several hundreds of micrometers. In Figure 5, a TEM micrograph of the interior of the coarse grain showing numerous fine  $\text{Cu}_9\text{Zr}_2$  precipitates is presented. Several coarse  $\text{Cu}_9\text{Zr}_2$  particles 1  $\mu\text{m}$  in size were also found in the specimens.

The microstructure of the alloy CuZr after one pass is presented on the micrograph in Figure 6(a). It consists

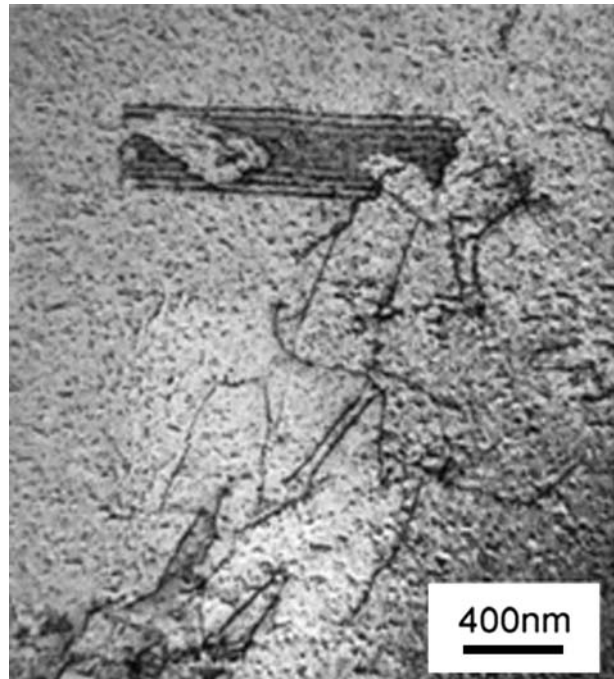


Fig. 5—Microstructure of the initial state of CuZr.

of elongated bands of cells and subgrains with a high density of dislocations in their interiors. The microstructure is very similar to that of pure copper (*cf.* Figure 4(a)) and confirms strong grain refinement during the first pass of ECAP.

Only minor changes in the microstructure occurred during the second pass of ECAP. The microstructure remains elongated, with dislocation cells or subgrains of small misorientation. A typical example of the structure is shown in Figure 6(b).

The microstructure of the specimen after four passes is shown in Figure 6(c) and clearly demonstrates changes that occurred in the material during the third and fourth pass of ECAP. The microstructure consists of subgrains with numerous well-defined boundaries closer to equilibrium, as compared to the specimens after one and two passes. The misorientation of these subgrains is much higher than in less strained specimens

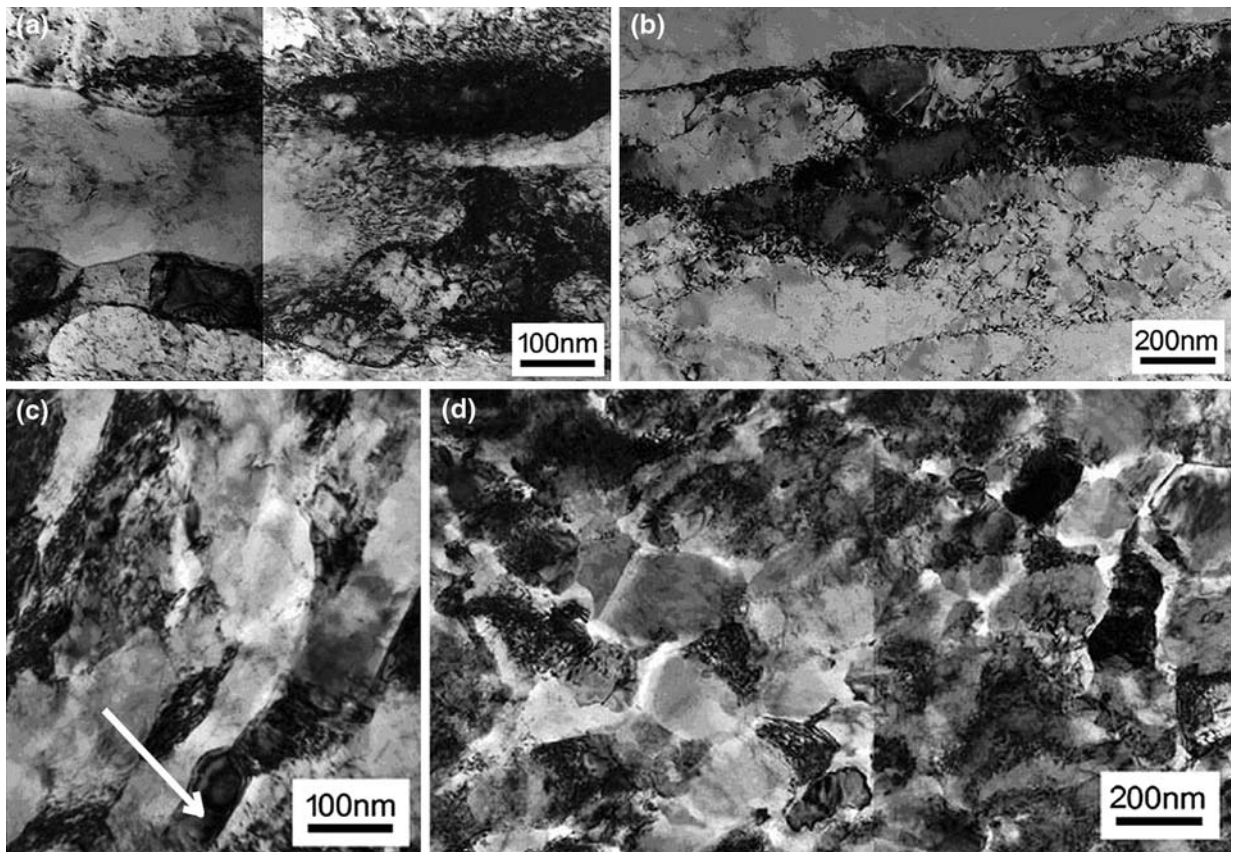


Fig. 6—Microstructure development during ECAP in CuZr specimens.

( $N = 1$  and  $2$ ). Moreover, the first recrystallized grains with a low density of dislocations and equilibrium boundaries were formed (marked with an arrow in the lower part of the micrograph). A significant reduction in the dislocation density also occurred. The average length of the still elongated grains/subgrains is 300 to 400 nm and the width is approximately 100 nm.

The typical microstructure of the CuZr specimen after eight passes is displayed in Figure 6(d). It consists largely of equiaxed grains with a high misorientation separated by GBs with a typical-thickness fringe contrast corresponding to the equilibrium boundaries. Several subgrains with nonsharp boundaries and a high density of dislocations can be also found in the specimen. The average size of the grains was 200 to 300 nm. Eight passes of ECAP resulted in strong grain refinement, by a factor of approximately 100.

### C. Electron Backscattered Diffraction

In both investigated materials, Cu and Cu-0.18 pct Zr, EBSD analysis showed that the original CG microstructure evolves from prolate bands of cells/subgrains enclosed by lamellar nonequilibrium GBs (after the first two ECAP passes) toward an equiaxed homogeneous microstructure with equilibrium GBs (after eight passes). Parts of measured maps presented in the form of inverse pole figures (IPFs) for the CuZr specimens after 1, 2, and 8 ECAP passes are shown in Figures 7(a), (b), and (c), respectively.

The grain/subgrain size distributions were determined from the measured maps using the line intercept method. As a boundary between the different grains or subgrains, misorientations of 15 or 2 deg, respectively, were adopted. The grain/subgrain size distributions follow the lognormal distribution, whereas the mean grain size decreases from approximately 10  $\mu\text{m}$  after the first ECAP pass to 460 nm after the eighth ECAP pass, in the Cu samples, and from approximately 12  $\mu\text{m}$  after the first ECAP pass to 260 nm after the eighth ECAP pass, in the case of the CuZr specimens. The mean subgrain size decreases from approximately 1  $\mu\text{m}$  for both materials after the first ECAP pass and approaches the mean grain size magnitude after eight ECAP passes. The plots of the mean grain/subgrain sizes as a function of the number of ECAP cycles are shown in Figures 8(a) and (b). The determined mean grain size in samples having an inhomogeneous microstructure (samples after the first and second ECAP passes consisting of elongated grains) can be understood only as a first rough approximation, because the mean grain size varies in different directions in the specimen (*cf.* Figure 7). The ECAP method resulted in a grain size reduction by a factor of approximately 100 after eight passes, for both the Cu and CuZr systems, in comparison to the original CG material; this confirms our TEM observations.

Orientation information obtained for each measured point of the EBSD map allows us to calculate the orientation relationship between pairs of distinct points,

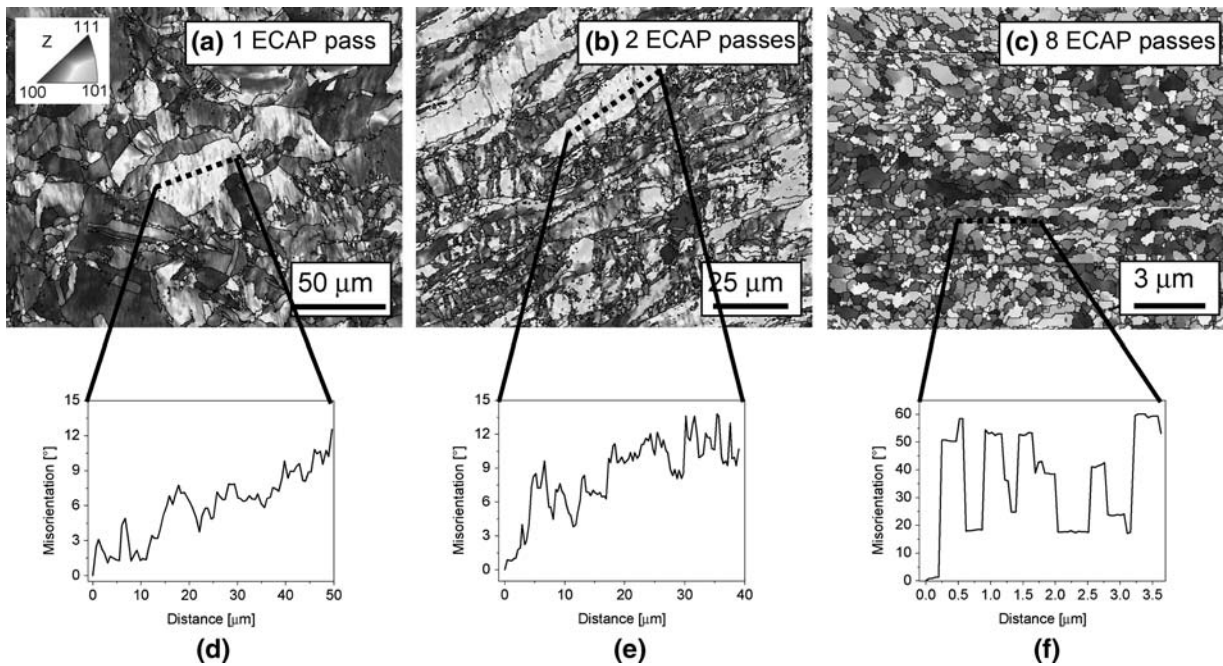


Fig. 7—Orientation maps of the CuZr samples in the IPF representation after (a) 1, (b) 2, and (c) 8 ECAP passes. The HAGBs (misorientation > 15 deg) are plotted as black lines. Misorientation profile through one deformed grain in  $N =$  (d) 1 and (e) 2 specimens and misorientation profile through several grains in  $N = 8$  specimen calculated around the dashed line indicated in the measured map (f).

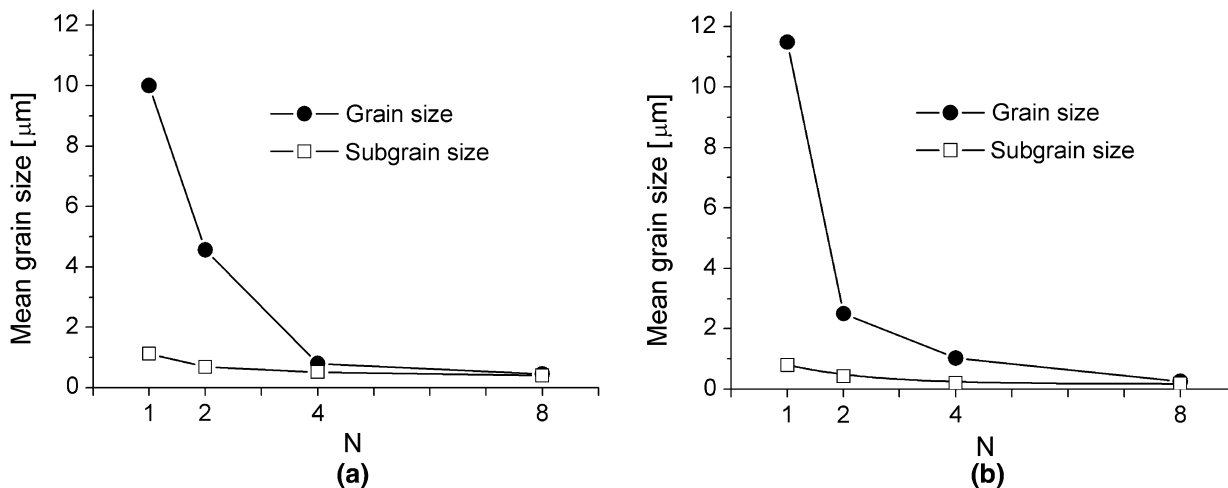


Fig. 8—Mean grain (●) and subgrain (□) size as a function of ECAP pass number determined from measured orientation maps using the line intercept method for (a) Cu and (b) CuZr samples.

the so-called misorientation. The correlated misorientation distribution based on the calculation of the misorientations between nearest-neighbor points therefore yields information about the character and fraction of the GBs, while for the calculation of the uncorrelated misorientation distribution, randomly chosen pairs of measured orientations are used that hold the information about the texture and morphology of the specimen. The misorientation distributions for the Cu sample after two ECAP passes are shown in Figure 9(a). From the misorientation distribution, the fraction of low-angle grain boundaries (LAGBs) and HAGBs can be determined. As a boundary between the LAGBs and HAGBs, the angle of 15 deg derived by Brandon<sup>[28]</sup> was chosen.

In Figures 9(b) and (c), the evolution of the LAGB/HAGB fractions for Cu and CuZr specimens as a function of the ECAP number is shown. A pronounced evolution from a high number of LAGBs to the higher number of HAGBs with increasing numbers of ECAP passes is clearly seen. After the first ECAP pass, more than 80 pct of the LAGBs were found in both the Cu and CuZr samples. With increasing strain (the increasing ECAP number), the fraction of the LAGBs decreases; after eight ECAP passes, the majority of GBs (more than 90 pct) are HAGBs in the Cu specimen. The decay of the LAGBs at the expense of the HAGBs is not as rapid in the CuZr samples (compare Figures 9(b) and (d)) and, finally, after the eighth ECAP

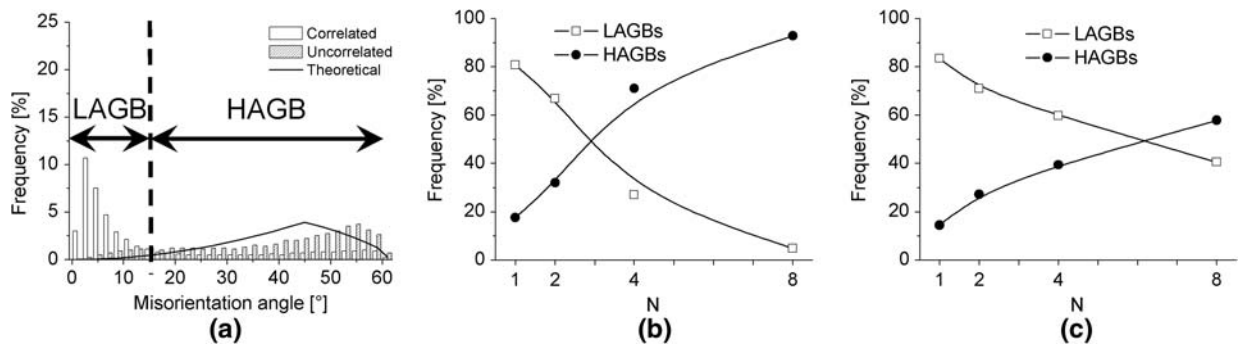


Fig. 9—Correlated (open bars), uncorrelated (hatched bars), and theoretical random-Mackenzie plot (solid line) distributions as functions of misorientation angles in (a) Cu specimen after two ECAP passes. The boundary between LAGBs and HAGBs (15 deg) is indicated in the plot. Frequency of appearance of LAGBs (□) and HAGBs (●) as a function of the number of ECAP passes for the (b) Cu and (c) CuZr specimens.

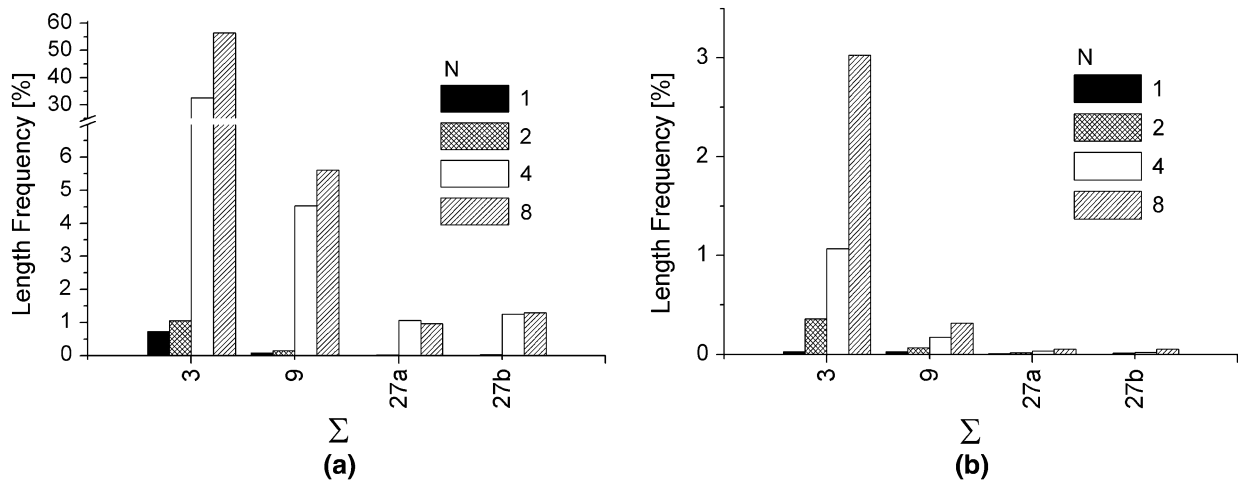


Fig. 10—Length frequency (in percent of total boundary length) of the  $\Sigma 3^n$  ( $\Sigma 3$ ,  $\Sigma 9$ , and  $\Sigma 27$ ) GBs as a function of the number of ECAP passes for the (a) Cu and (b) CuZr specimens.

cycle, the LAGB/HAGB ratio is 42/58 pct in the CuZr specimen.

The uncorrelated misorientation distributions approach the random theoretical distribution (Mackenzie plot: the solid line in Figure 9(a))<sup>[29]</sup> with increasing ECAP straining, for both the Cu and CuZr specimens. This is a consequence of the sample structure homogenization that occurs during ECAP processing.

The evolution of the HAGBs during the ECAP straining (in details discussed in Reference 30) can be described using the grain-boundary distribution by the reciprocal density of coincidence sites  $\Sigma$  (CSL) theory. The Brandon criterion  $\Delta\theta = \theta_0 \Sigma^{-1/2}$ ,<sup>[26]</sup> in which  $\Delta\theta$  is the deviation from the exact CSL angle,  $\theta_0$  is the LAGB/HAGB limit, and  $\Sigma$  is the corresponding CSL, was adopted as a tolerance limit from the exact CSL values. In both the Cu and CuZr samples, we can observe a pronounced increase in the  $\Sigma 3^n$  (e.g.,  $\Sigma 3$ ,  $\Sigma 9$ , and  $\Sigma 27$ ) GBs with increasing ECAP passes. In the CuZr samples, the increase in the  $\Sigma 3^n$  GBs is smooth and continuous, with approximately 3 pct of the  $\Sigma 3$  GBs after eight ECAP passes. In Cu, however, the evolution is similar for the first two ECAP passes only, while a dramatic

increase in the  $\Sigma 3^n$  GBs occurs after the fourth and eighth ECAP passes. Less than 1 pct of  $\Sigma 3$  boundaries were found after the first pass, while nearly 60 pct were found in the specimen after eight ECAP passes. This significant development of the  $\Sigma 3^n$  is displayed in Figures 10(a) and (b).

Enhanced twinning in severe plastically deformed Cu by high-pressure torsion (HPT) and ECAP was also reported by many authors.<sup>[17,31,32]</sup> This somewhat surprising mechanism, which is usually not observed at the ambient temperature in CG Cu due to a sufficient number of slip systems, becomes favorable after a substantial strain hardening once a critical dislocation density is reached.<sup>[33,34]</sup> This condition is met in our specimens already after the first pass of ECAP; deformation twins can therefore be favored over dislocation slip in areas in which high strains are locally reached. Randle<sup>[35]</sup> claimed that  $\Sigma 3$  boundaries may have different geometries and may comprise both coherent and incoherent twins or stacking faults.

The deformation state of the specimen can be roughly estimated from the EBSD measurements. Based on the orientation mapping, we first reconstruct the individual

grains, then estimate the average orientation in each grain, and finally calculate the deviations from this average orientation within the grain. When the deviations from the average orientation exceed the defined limit, the grain is assumed to be deformed; otherwise, the grain is described as recrystallized. In Figures 11(a) and (b), the deformation state of the specimen as a function of the ECAP passes is shown. In both the Cu and CuZr, the specimens were already in a deformed state after the first ECAP pass. This corresponds to the fragmentation of the initial coarse grains during the ECAP passing, compared with the misorientation profile measured through one grain in Figure 7(a). In the Cu specimen, the recrystallized fraction of the sample increases with increasing ECAP straining, whereas a steep increase in recrystallized grains after the fourth ECAP pass occurs. After eight passes, the ratio between the deformed and recrystallized fraction of the sample is 18/82 pct. In the CuZr specimen, the recrystallized fraction increases after the second ECAP pass. Unlike the Cu specimen, however, the CuZr specimen does not exhibit pronounced evolution with subsequent ECAP straining and the ratio between the deformed and recrystallized fraction is approximately 90/10 pct after eight passes.

#### D. Positron Annihilation Spectroscopy

A well-annealed Cu sample not subjected to ECAP (zero passes) exhibits a single component with the lifetime  $\tau_B = 114$  ps (Table III), which agrees well with the calculated lifetime of free positrons in a perfect Cu crystal.<sup>[36]</sup> Hence, the defect density in the well-annealed Cu specimen is very low and virtually all positrons annihilate from the free, delocalized state. Due to the fact that no positron trapping at dislocations was

observed (*i.e.*, the dislocation density is below the lower sensitivity limit of PL spectroscopy), we can estimate that the mean dislocation density in the virgin Cu does not exceed  $10^{12} \text{ m}^{-2}$ .

The PL results for the virgin Cu-0.18 pct Zr specimen not subjected to ECAP (zero passes) are shown in Table III, as well. The specimen exhibits a two-component PL spectrum with lifetimes  $\tau_1$ ,  $\tau_2$  and relative intensities  $I_1$ ,  $I_2$ . The shorter component with the lifetime  $\tau_1 < \tau_B$  obviously comes from free positrons not trapped at defects. The shortening of  $\tau_1$  with respect to the lifetime  $\tau_B$  of free positrons in a perfect Cu crystal is due to positron trapping at defects and is explained by the well-known simple trapping model (STM).<sup>[36]</sup> The longer component with the lifetime  $\tau_2 \approx 164$  ps can be attributed to positrons trapped at dislocations.<sup>[37]</sup> The mean dislocation density  $\rho_D$  in the virgin CuZr specimen can be determined using the two-state STM:<sup>[20]</sup>

$$\rho_D = \frac{1}{v_D} \frac{I_2}{I_1} \left( \frac{1}{\tau_B} - \frac{1}{\tau_2} \right) \quad [1]$$

where  $v_D = 0.6 \times 10^{-4} \text{ m}^2 \text{ s}^{-1}$  is the specific positron trapping rate for Cu dislocations.<sup>[38]</sup> The dislocation density calculated using Eq. [1] for the Cu-0.18 pct Zr virgin specimen is listed in Table IV.

In the framework of STM, the quantity  $\tau_f$  defined as

$$\tau_f = \left( \frac{I_1}{\tau_1} + \frac{I_2}{\tau_2} \right)^{-1} \quad [2]$$

equals the lifetime of free positrons in a perfect Cu crystal, *i.e.*,

$$\tau_f \equiv \tau_B \quad [3]$$

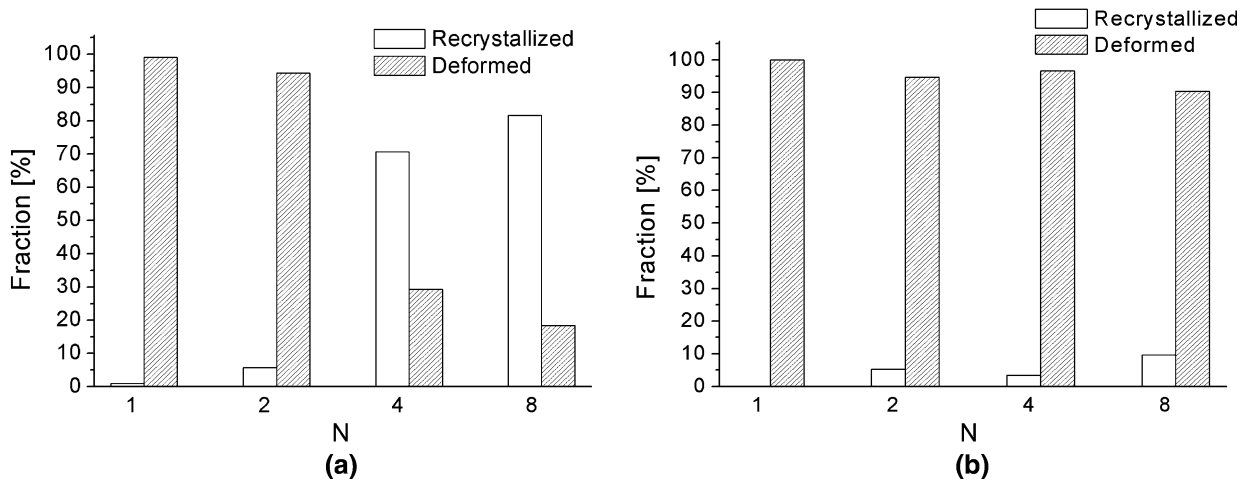


Fig. 11—Recrystallized (open bars) and deformed (dashed bars) fraction of the sample as a function of ECAP passes number for the (a) Cu and (b) CuZr specimens.

Table III. PL Results for Virgin Specimens Not Subjected to ECAP

Sample	$\tau_1$ (ps)	$I_1$ (Pct)	$\tau_2$ (ps)	$I_2$ (Pct)	$\tau_f$ (ps)
Cu	$114 \pm 1$	100	—	—	—
Cu-0.18Zr	$109.6 \pm 0.7$	$87.5 \pm 0.8$	$164 \pm 2$	$12.5 \pm 0.8$	$114 \pm 1$

The condition [3] is a useful test of the consistence of the decomposition of the PL spectrum with the STM. The quantity  $\tau_f$  calculated from Eq. [2] is shown in Table III. The condition [3] is satisfied for the CuZr specimen. This

**Table IV. Mean Dislocation Densities  $\rho_D$  and Concentrations of Microvoids  $c_V$  Estimated from PL Data**

Sample	Number of Passes ( $N$ )	$\rho_D$ ( $m^{-2}$ )	$c_V$ ( $at^{-1}$ )
Cu	0	$\leq 10^{12}$	$< 10^{-6}$
Cu	1	$\geq 5 \times 10^{14}$	$\geq 1 \times 10^{-4}$
Cu	2	$\geq 5 \times 10^{14}$	$\geq 1 \times 10^{-4}$
Cu	8	$\geq 5 \times 10^{14}$	$\geq 5 \times 10^{-5}$
Cu-0.18Zr	0	$(8 \pm 1) \times 10^{12}$	$< 10^{-6}$
Cu-0.18Zr	1	$\geq 5 \times 10^{14}$	$\geq 1 \times 10^{-5}$
Cu-0.18Zr	2	$\geq 5 \times 10^{14}$	$\geq 1 \times 10^{-5}$
Cu-0.18Zr	4	$\geq 5 \times 10^{14}$	$\geq 5 \times 10^{-5}$
Cu-0.18Zr	8	$\geq 5 \times 10^{14}$	$\geq 5 \times 10^{-5}$

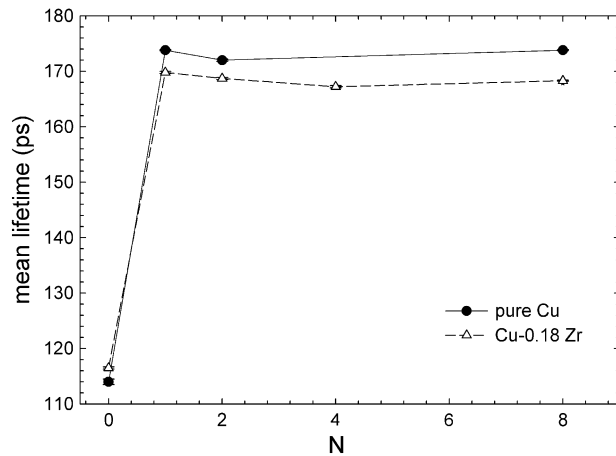


Fig. 12—Mean PL as a function of the number of ECAP passes for both materials studied.

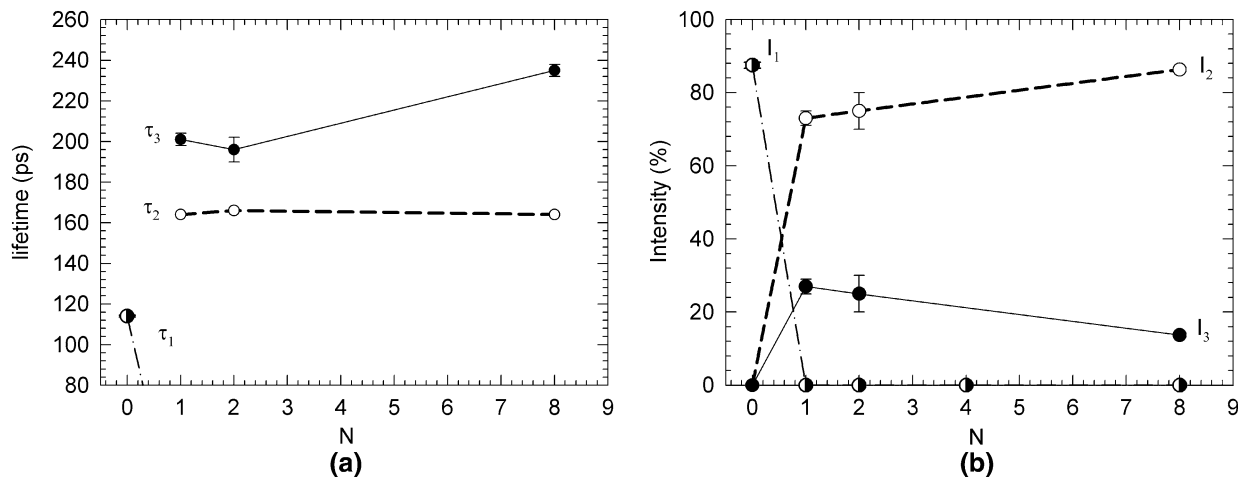


Fig. 13—PL results for Cu subjected to various numbers of ECAP passes: (a) lifetimes of the components resolved in PL spectra and (b) corresponding relative intensities (half-filled circles =  $\tau_1$ ,  $I_1$  (free positrons), open circles =  $\tau_2$ ,  $I_2$  (dislocations), and full circles =  $\tau_3$ ,  $I_3$  (microvoids)).

confirms that the assumptions of the two-state STM (a single type of uniformly distributed defects, no detrapping, etc.) are fulfilled and that Eq. [1] can be used for evaluation of the mean dislocation density.

### E. Specimens Deformed by ECAP

The mean PL:

$$\bar{\tau} = \sum_i \tau_i I_i \quad [4]$$

where  $\tau_i$ ,  $I_i$  are the lifetimes and relative intensities of the components resolved in the PL spectra, is a robust integral parameter that is only slightly influenced by the mutual correlations of the fitted parameters. Figure 12 shows the dependence of the mean PL on the number of ECAP passes, for all the materials studied. One can see in the figure that the specimens deformed by ECAP exhibit a significantly higher mean PL. The behavior of the mean lifetime with an increasing number of passes is similar in all studied materials: There is a huge increase in the mean PL after the first ECAP pass, followed by only small variations for higher numbers of passes. This confirms the fact that a large concentration of defects is introduced by severe plastic deformation during the first pass.

The PL spectra of the specimens subjected to ECAP deformation consists of the following two components: (1) a component with an intensity  $I_2$  and a lifetime  $\tau_2 \approx 164$  ps, which is known to represent a contribution of positrons trapped at dislocations,<sup>[36]</sup> and (2) a longer component with a lifetime  $\tau_3$  and an intensity  $I_3$ , which can be attributed to positrons trapped at small vacancy clusters called microvoids<sup>[39]</sup> that are often detected in UFG metals prepared by severe plastic deformation. It is assumed that microvoids were formed by the clustering of vacancies created during ECAP deformation. The behavior of PLs  $\tau_i$  and the relative intensities  $I_i$  of the components resolved in the PL spectra of pure Cu and CuZr specimens are plotted in Figures 13 and 14,

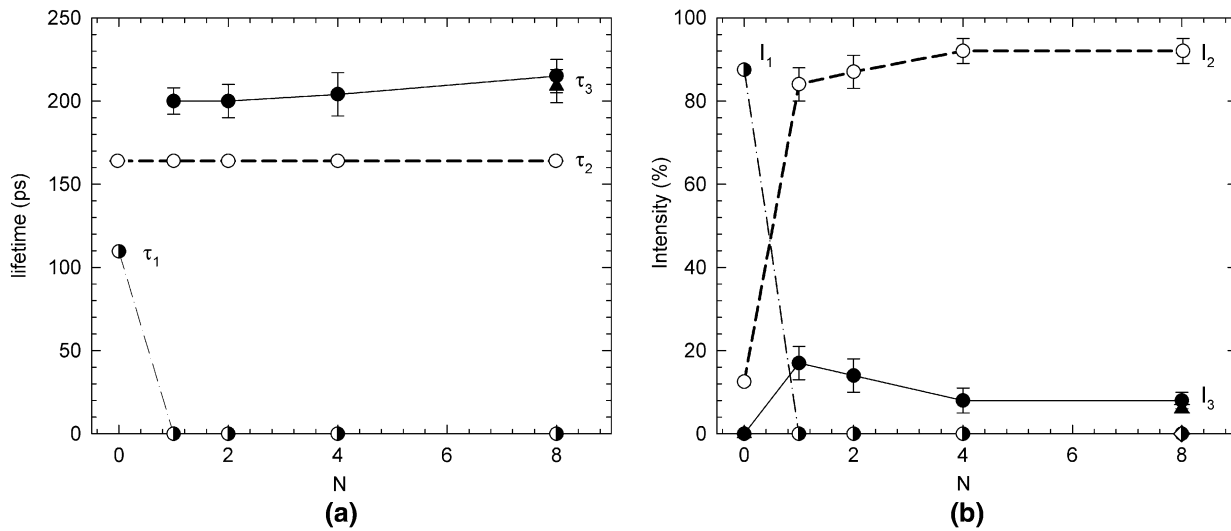


Fig. 14—PL results for CuZr alloy subjected to various number of ECAP passes: (a) lifetimes of the components resolved in PL spectra and (b) corresponding relative intensities (half-filled circles =  $\tau_1$ ,  $I_1$  (free positrons), open circles =  $\tau_2$ ,  $I_2$  (dislocations), and full circles =  $\tau_3$ ,  $I_3$  (microvoids)).

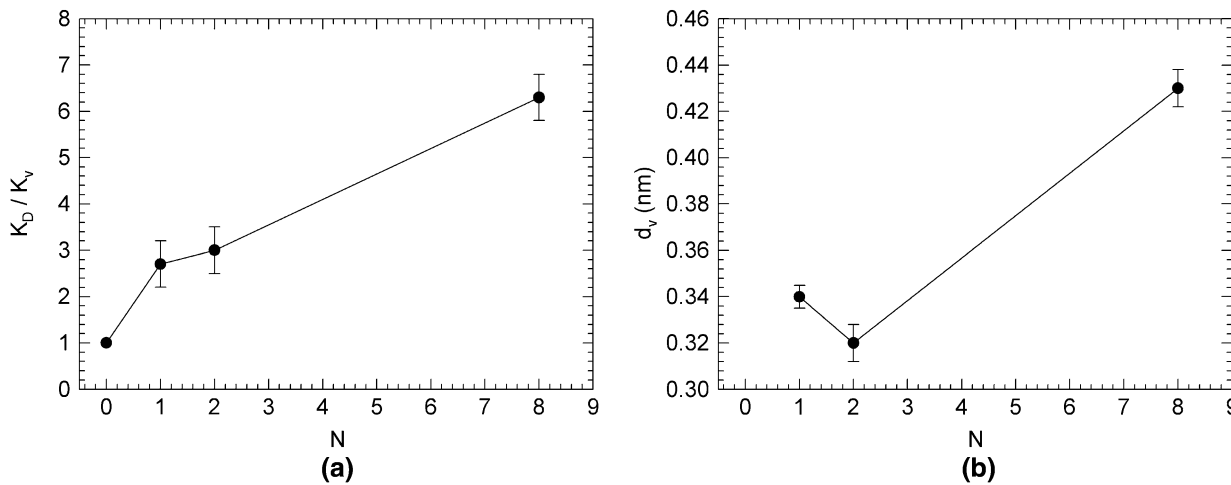


Fig. 15—ECAP-deformed pure Cu specimens: (a) ratio  $K_D/K_v$  of positron trapping rates to dislocations and microvoids and (b) diameter of microvoids calculated from PAS results.

respectively, as a function of the number of ECAP passes. The free positron component with a lifetime  $\tau_1$  and intensity  $I_1$  disappeared in the ECAP-deformed specimens. Therefore, ECAP-deformed materials contain a very high density of defects. Practically all positrons are trapped at defects and annihilate from a localized state in some defect (the so-called saturated positron trapping). Dislocations are dominant defects in the specimens deformed by ECAP. One can estimate that the mean dislocation density in ECAP-deformed samples exceeds  $5 \times 10^{14} \text{ m}^{-2}$ . The estimated dislocation density and concentration of microvoids are shown in Table IV. The behavior of intensities  $I_2$  and  $I_3$  in specimens subjected to more than one ECAP pass reflects changes in the ratio of the two competing traps existing in the specimens: dislocations and microvoids.

One can see in Figures 13 and 14 that ECAP-deformed pure Cu and CuZr alloys exhibit similar

behavior with increasing number of passes. The contribution of positrons trapped at dislocations increases with increasing number of passes, while the intensity of positrons trapped at microvoids had already reached a maximum after the first ECAP pass and gradually decreased with further increase in the number of passes. Because of the saturated positron trapping in defects ( $I_1 = 0$  pct), the ratio of the intensities of the trapped positrons is equal to the ratio of positron trapping rates to the corresponding defects, which is directly proportional to the ratio of defect densities,<sup>[36]</sup> *i.e.*,

$$\frac{I_2}{I_3} = \frac{K_D}{K_v} \sim \frac{\rho_D}{c_v} \quad [5]$$

The ratios of  $K_D/K_v$  for ECAP-deformed pure Cu and CuZr alloys as a function of the number of passes are plotted in Figures 15(a) and 16(a). It is clearly seen that

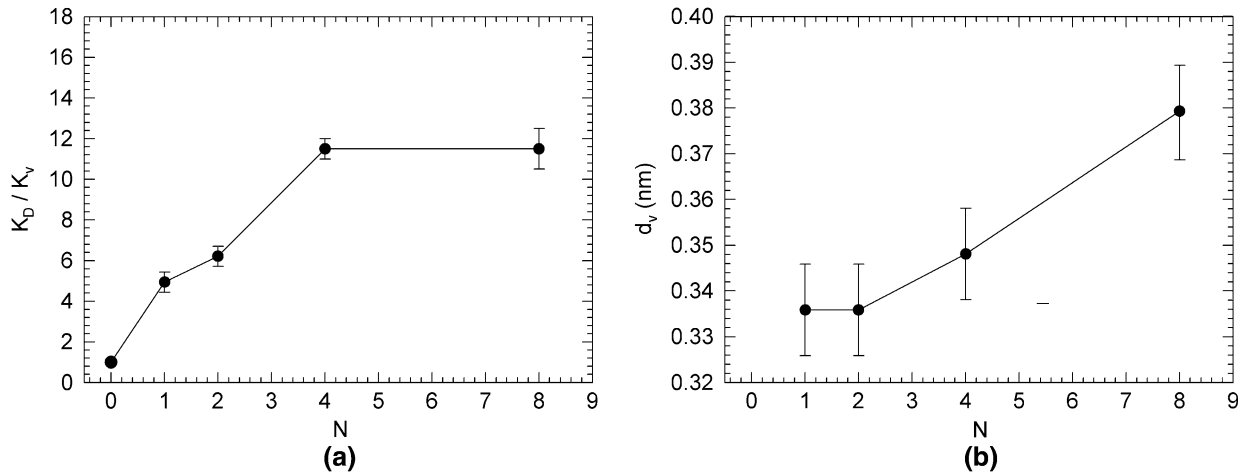


Fig. 16—ECAP-deformed CuZr alloy: (a) ratio  $K_D/K_V$  of positron trapping rates to dislocations and microvoids and (b) diameter of microvoids calculated from PAS results.

the dislocation density in the specimens deformed by ECAP increases with an increasing number of passes more quickly than does the concentration of microvoids.

By comparing the lifetime  $\tau_3$  of the component arising from the microvoids with the theoretical calculations performed in Reference 39, one can determine the size of these defects. The results of these calculations for ECAP-deformed pure Cu and CuZr alloys are displayed in Figures 15(b) and 16(b), in which the microvoid diameter  $d_V$  is plotted as a function of the number of ECAP passes. Microvoids are very small defects having the size of  $\approx 2$  monovacancies in the specimens subjected to a single ECAP pass. With an increasing number of passes, the size of the microvoids increases and, in the samples subjected to eight ECAP passes, becomes comparable to  $\approx 4$  monovacancies.

## F. XRD Line-Profile Analysis

### 1. Simplified integral breadth methods

The first version of the method includes the fitting of experimental profiles with the Pearson VII or pseudo-Voigt functions using the program DIFPATAN (developed by R. Kužel).<sup>[40]</sup> The correction for instrumental broadening was performed with the aid of a NIST LaB<sub>6</sub> standard and the Voigt function method.<sup>[41]</sup> The method consists of the separation of an integral breadth of both the standard and measured profiles into the Gauss and Cauchy components, their subtraction in linear (Cauchy) and quadratic (Gauss) form, and the synthesis yielding the total integral breadth corrected for instrumental broadening. The second version of the method directly fits the convolution of instrumental and physical functions and is described in Reference 42. The method is often visualized in terms of the Williamson–Hall plot (integral breadth  $\beta$  (in  $1/d$ ) vs  $\sin \theta$ ), the intercept of which indicates that the reciprocal value of the mean crystallite size and the slope is proportional to the microstrain (or the square root of the dislocation density). For the Cu samples subjected to ECAP, the strain broadening is dominating and the crystallite size was beyond the sensitivity limit of the method, *i.e.*, a few

hundreds of nanometers. In this case, a formula derived by Krivoglaž<sup>[43,44]</sup> could be used for the integral breadth. However, it is not appropriate for highly correlated dislocations. A similar approximate formula given in Reference 45 was applied instead:

$$\beta_{hkl} = \sqrt{\rho \chi_{hkl}} f(M) \frac{\sin \theta}{\lambda} \quad [6]$$

where  $\mathbf{b}$  is the size of the Burgers vector of assumed dislocations,  $\lambda$  is the wavelength,  $\theta$  is the diffraction angle, and  $\chi_{hkl}$  is the so-called orientation or contrast factor determining the line-broadening anisotropy. It depends on the particular slip system, the dislocation character, the elastic anisotropy, and the orientation of the diffraction vector with respect to the Burgers vector and the dislocation line. The main limitation of the method is the uncertainty of the correlation parameter of the dislocation arrangement, which is related to the line-profile shape. This value is often written as  $M = r_c \sqrt{\rho}$ , where  $r_c$  denotes the outer cutoff radius of dislocation strain field and  $\rho$  is the dislocation density. An analytic approximation of the  $f(M)$  function is given in Reference 45, as follows:

$$f(M) = a \ln(M+1) + b \ln^2(M+1) + c \ln^3(M+1) + d \ln^4(M+1) \quad [7]$$

where  $a = -0.173$ ,  $b = 7.797$ ,  $c = -4.818$ , and  $d = 0.911$ .

The  $M$  factor can be estimated from the line shape, for example, in terms of the Voigt function approximation (the ratio of the long-tailed Lorentzian component of the breadth to the short-tailed Gaussian one ( $y = \beta_c / \sqrt{\pi} \beta_g$ )). Based on the data shown in Reference 45, one can use an approximate relation  $M = 1/y$ . More precisely, the data can be fitted with the formula  $M = 0.96/y^{0.95}$ . The formula should be applied after the correction of the instrumental broadening using the Voigt function, which gives corrected values of  $\beta_c$ ,  $\beta_g$ . Even though the factors vary with  $hkl$  indices, a mean value of the  $M$  factor averaged over all reflections was always used. The reason was that the individual factors

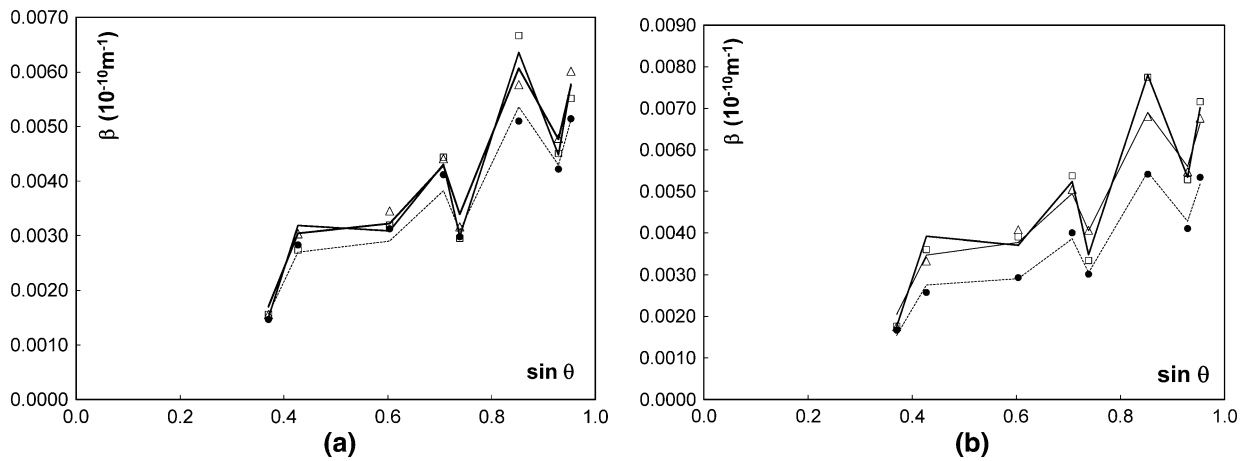


Fig. 17—Williamson–Hall plot (integral breadth  $\beta(1/d)$  vs  $\sin \theta$  with indicated  $hkl$  indices for ECAP copper samples: one pass =  $\bullet$ , dashed line; two passes =  $\Delta$ , thick line; eight passes =  $\square$ , thin line. Symbols correspond to experimental data after instrumental correction. Lines connect corresponding calculated values: (a) Cu and (b) CuZr.

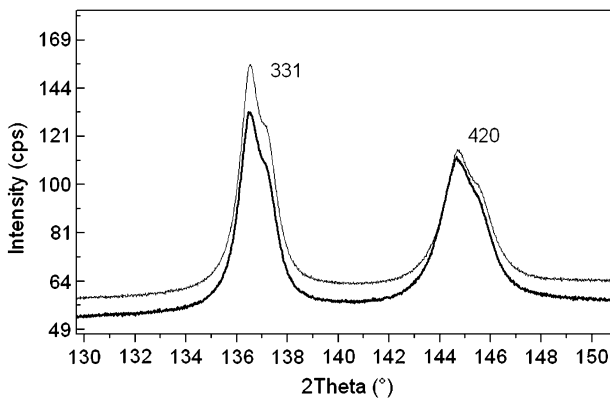


Fig. 18—High-angle diffraction peaks for ECAP Cu samples after one pass (upper thin line) and eight passes (lower thick line). Both the line-broadening anisotropy (narrower line 331) and the change in line shape (longer tails for eight passes) can be seen.

obtained by the procedure described earlier are influenced significantly by experimental (statistical) errors, because each factor depends on four experimental values and their ratios (Gauss and Cauchy components of both instrumental and experimental profiles) and, consequently, may introduce more noise in otherwise quite stable experimental values of integral breadths.

Modified Williamson–Hall plots (integral breadth  $\beta$  vs  $\sin \theta$ ) do not show a significant dependence on  $n_p$ , except for the slightly varying typical line-broadening anisotropy of the  $\beta_{hhh} \ll \beta_{h00}$  type. Such anisotropy (Figure 17) can be well explained by the orientation factors calculated assuming only dislocations with the Burgers vector  $\mathbf{b} \parallel \langle 110 \rangle$  that are typical for fcc structures. The anisotropy is closely related to the elastic anisotropy of copper. The correspondence between the calculated and experimental values was good in most cases (Figures 17(a) and (b)). However, high-quality data allow us to see changes in the line shape (Figure 18). With increasing number of ECAP passes, the profile tails are longer and the profile shape is more Lorentzian. This is confirmed by the fitting of the Pearson VII function to experimental profiles (decreasing exponent  $n$ ), or by increasing the  $y$  ratio obtained for physical profiles. Consequently, the estimated  $M$  parameter decreases with an increasing number of passes. This can be caused by a higher correlation in the dislocation densities or twins and is in agreement with the TEM and EBSD results.

In the first approximation, the fractions of the edge and screw dislocations can be taken as equal. However, better fits can be obtained for the nonequal fractions. In particular, the fraction of the edge dislocations seems to decrease with the number of passes (Table V). Actually,

Table V. Structure Parameters for ECAP Cu Samples Measured at Transversal Direction and Different Numbers of Passes (1, 2, and 8)\*

Sample	$\rho_\beta, 10^{15} \text{ m}^{-2}$	$\rho_{\text{TPF}}, 10^{15} \text{ m}^{-2}$	$w$	$M_\beta$	$M_{\text{TPF}}$	$\langle L \rangle$ (nm)
Cu-1	2.1	2.1	0.95	1.4	0.47	78
Cu-2	3.1	6.6	0.85	1.1	0.28	71
Cu-8	8.0	7.9	0.35	0.7	0.25	76
CuZr018: $N = 1$	1.2	1.9(2)	0.83(5)	1.9	0.63(8)	70(9)
CuZr018: $N = 2$	2.2	2.7(3)	0.90(6)	1.6	0.76(11)	70(9)
CuZr018: $N = 4$	2.9	3.0(4)	0.42(6)	1.4	0.81(11)	75(6)
CuZr018: $N = 8$	4.3	3.9(6)	0.23(10)	1.0	0.61(14)	73(8)

\* $\rho_\beta$  is the dislocation density obtained by the simplified method;  $\rho_{\text{TPF}}$  is the dislocation density from total-pattern fitting;  $w$  is the fractions of edge dislocations;  $M_\beta M$  factor is estimated from the  $y$  ratio;  $M_{\text{TPF}} M$  factor is obtained by the fitting;  $\langle L_{\text{TPF}} \rangle$  is the mean crystallite size obtained by total-pattern fitting. Statistical errors obtained from a set of measurements and a set of fits were evaluated for total-pattern fitting method.

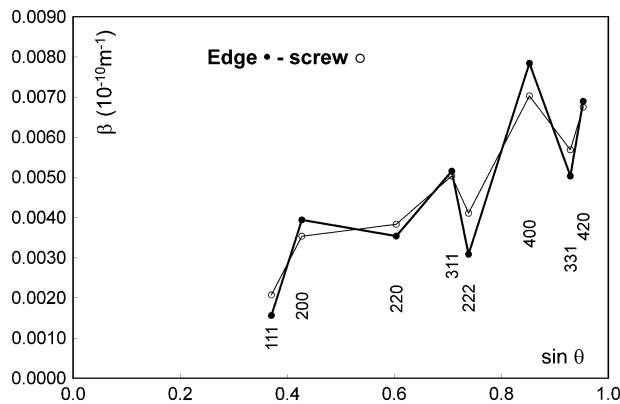


Fig. 19—Illustration of the influence of the fraction of edge and screw dislocations with the Burgers vector  $a/2\langle 110 \rangle$  on the XRD line-broadening anisotropy in the Williamson–Hall plot (integral breadth  $\beta(1/d)$  vs  $\sin \theta$  for Cu ( $\bullet$  = 100 pct screw;  $\circ$  = 100 pct edge).

this parameter for the considered slip system determines the magnitude (not the type, in this case) of line-broadening anisotropy, regardless of its interpretation, and it slightly increases with the number of passes. However, the sensitivity of the line-broadening anisotropy to the fraction of the edge and screw dislocations is not very high in this particular case (Figure 19), and unambiguous conclusions must therefore be drawn with caution.

## 2. Total-pattern fitting

In this procedure, essentially four to five free parameters are used: the dislocation density, dislocation correlation factor, mean crystallite size, variance in the size distribution, and/or the fraction of screw and edge dislocations. An extended FOX program was used for the fitting.<sup>[23]</sup> The program also includes different types of corrections (absorption, thin films samples, textures, stresses, and peak shifts), the size broadening in terms of log-normal size distribution, and the phenomenological microstrain or dislocation model. The more user-friendly program of Matteo Leoni,<sup>[46–48]</sup> which includes a large variety of size distributions and also a dislocation model, may also be used for the fitting, instead.

The procedure of total-pattern fitting was always carried out by reducing the  $M$  factor (in particular,  $r_c$ ), in order to fit long tails. The values of the dislocation densities were in surprisingly good agreement with the former integral breadth method. On the other hand, the determined crystallite size was below 100 nm and did not change with the number of passes. Rather small values of crystallite size is a typical feature of all Fourier-type (and derived total-pattern fitting type) methods used for deformed materials. Such small values often have no direct evidence either in TEM or in EBSD. In spite of a clear distinction in the definition (XRD crystallite: coherently diffracting domain), the effect should be further studied. Moreover, it must be noted that the simplified method is much more robust but also more approximate, and that, for a higher dislocation correlation (small  $M$ ), underestimates the

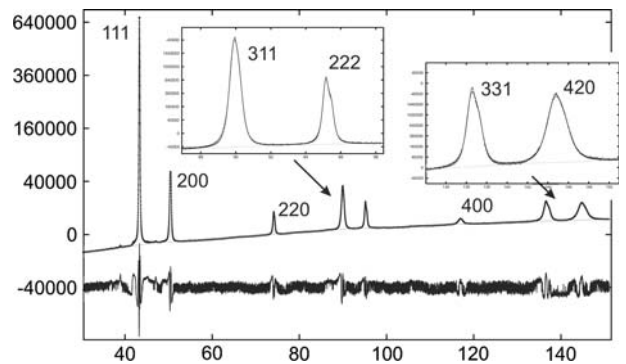


Fig. 20—Total-pattern fitting of CuZr diffraction pattern after one ECAP pass by extended FOX program. Details of fits for two pairs of diffraction profiles are shown.

size effect (the Williamson–Hall plot is not linear at low  $\theta$  values). By contrast, the total-pattern fitting uses all the information, but the correlation of parameters may be a problem and the fits are not ideal because of the long tails and small asymmetry of some of the experimental diffraction profiles. Attempts to fit such profiles with a function, including stacking faults (twins), have not been successful. An example of the fit is shown for the CuZr sample after one pass in Figure 20. The overall fit is usually quite good (profile  $R_w$  factors are usually in the range 1 to 2 pct), but, in the details, small discrepancies in peak tails or a peak top can be discovered. It seems that the current theoretical model of dislocation line broadening cannot completely describe the microstructure of the copper samples processed by ECAP. Nevertheless, reasonable and useful results, in particular, concerning the dislocation density evolution, were obtained.

All values of the crystallite size obtained by total-pattern fitting are approximately 70 nm. Due to the variation in  $M$ , the dislocation density increases with the number of passes, in agreement with PL measurements. It must be noted, however, that the uncertainty in the dislocation densities increases with a decreasing  $M$  factor, due to larger errors in its determination below  $M \sim 0.5$  (eight passes, pure Cu), as it also follows from the dependence on the profile shape ( $M = 1/y$ ) described earlier. The errors can then reach the tens of percents.

Unlike Reference 34, the results for CuZr in Table V were obtained by averaging several measurements of samples that were also from different planes ( $X$ ,  $Y$ , and  $Z$ ) and after several fits. Hence, the texture, which is quite significant for the ECAP samples, caused different weights of individual diffraction peaks (Figure 21) in different fits and, therefore, the fits may be sensitive to different features of the pattern. However, in general, the same dislocation densities were obtained. Only small differences in the line-broadening anisotropy were observed for different sample planes and with slightly smaller values for plane  $Z$ . Detailed studies together with detailed texture analysis are still in progress.

The lattice parameters of all the samples investigated agreed well with the tabulated values. This indicates the absence of significant residual stresses.

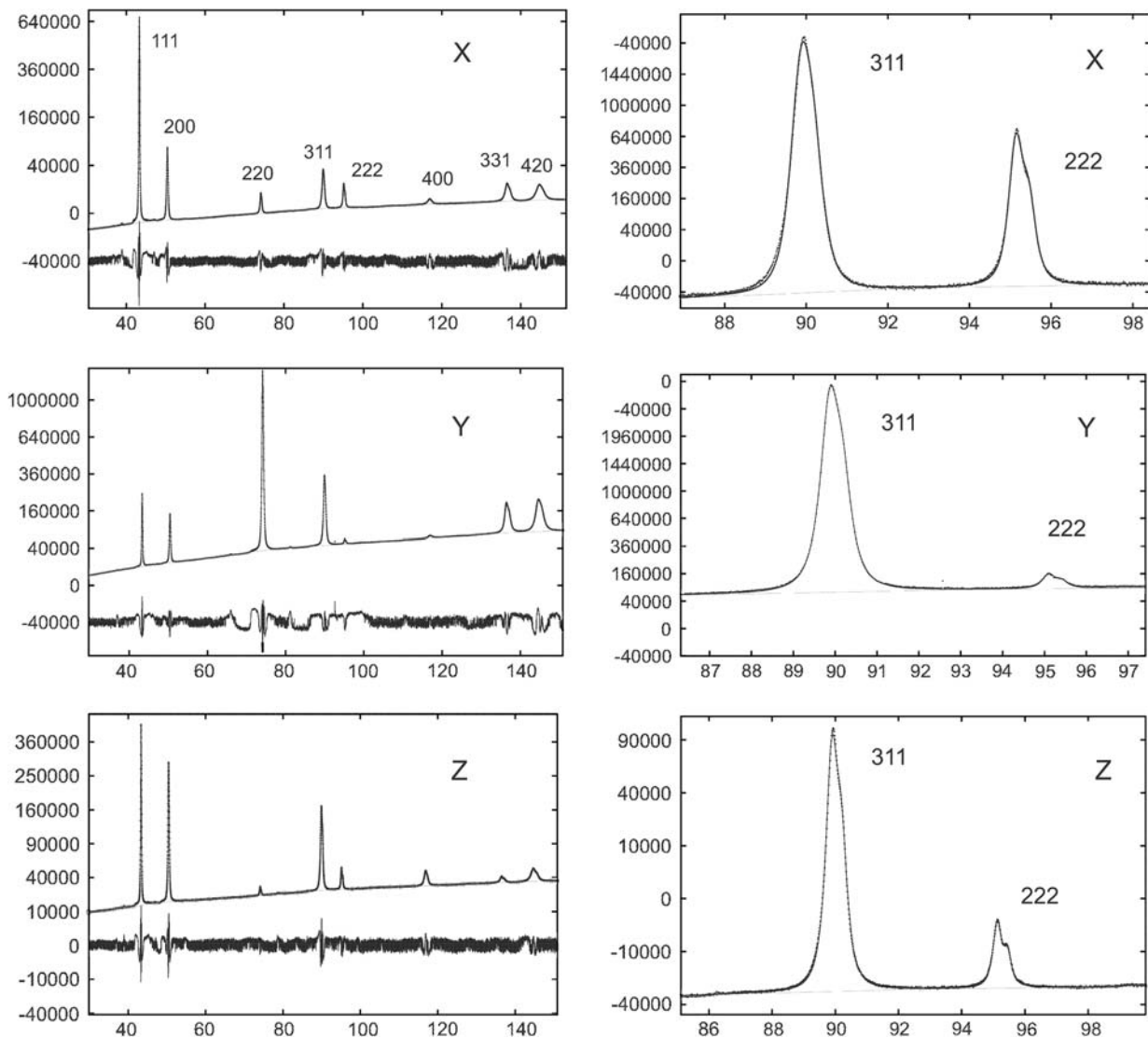


Fig. 21—Total-pattern fitting of CuZr diffraction patterns after one ECAP pass taken from different planes of sample (*X*, *Y*, and *Z*). The ratio of peak intensities is significantly changed due to the texture. Right column shows details of fits for 311 and 222 diffraction profiles.

#### IV. SUMMARY

The microstructure evolution in UFG Cu and CuZr polycrystals prepared by ECAP was studied using various experimental techniques.

Significant changes in microstructure with the number of ECAP passes were observed by both TEM and EBSD. The findings of both methods were in agreement.

The ECAP processing (straining) leads to the shearing of grains, accompanied by an increase in the fraction of LAGBs after the first ECAP pass. Increasing deformation results in an increase in misorientations within the deformation bands and in the formation of new HAGBs. The GB distribution changed from the high portion of LAGBs after the first two ECAP passes to the high portion of HAGBs after eight passes. In combination with a sample rotation of approximately 90 deg around the extrusion direction (route *B<sub>c</sub>*) after each ECAP pass, ECAP causes polygonization and the transformation of the substructure into a granular-type microstructure

accompanied by a dramatic grain-size reduction. The grain size decreased approximately 100 times with respect to the original material.

The significant dependence of twinning on the applied strain (the number of ECAP passes) was found in our specimens. Moreover, in Cu, we observed the formation of a high fraction of twin-related  $\Sigma 3''$  ( $\Sigma 3$ ,  $\Sigma 9$ , and  $\Sigma 27$ ) GBs; this effect was found only insignificantly in the CuZr alloy, however.

The differences in the behavior of the Cu and CuZr specimens subjected to ECAP processing can be explained on the basis of the TEM results. In the CuZr alloy, numerous tiny  $\text{Cu}_9\text{Zr}_2$  precipitates were observed. We assume that these precipitates block the movement of the dislocation walls (boundaries), which manifests itself in a significantly reduced fraction of HAGBs after eight ECAP passes in CuZr as compared to Cu.

The PL and XRD methods are sensitive to different microstructural features. The former method revealed

the presence of microvoids the size of which increases from two monovacancies after one pass to four monovacancies after eight passes. Even though the dislocation density was too high to be determined by PL, a slight increase in the intensity corresponding to dislocations with the number of passes was observed. This is in good correspondence with the results of the XRD line-profile analysis performed by several methods. In contrast to PL, XRD line-profile analysis is sensitive to high dislocation densities and allows their quantitative determination. The values are in the range  $2$  to  $4 \times 10^{15} \text{ m}^{-2}$ , in rough agreement with the densities obtained in Reference 49. Our values are slightly higher, but it must be noticed that we used a copper sample with lower purity. A small increase in the values with the number of passes is accompanied by a variation in the dislocation-correlation parameter  $M$  (or dislocation cutoff radius). Its drop after eight passes, *i.e.*, the increase in correlation in the dislocation arrangement, could be detected, in particular, for pure copper. A systematic increase in XRD line-broadening anisotropy with the number of passes was observed; this could correspond to the increase in the fraction of the screw dislocations. However, this may also be related to the changes in texture. Such analysis is still in progress. For the investigated ECAP samples, the XRD line broadening is mainly dislocation induced and the values of the dislocation densities obtained by different methods (the approximate integral breadth method and the total pattern fitting) were in good agreement. This is not true for minor effects of the so-called size broadening or for the dislocation-correlation parameter, which is sensitive to line shape. However, in the latter case, the trends with increasing numbers of passes can be well followed.

## ACKNOWLEDGMENTS

This work was financially supported by the research program MSM 0021620834 of the Ministry of Education of the Czech Republic. One of the authors (OS) acknowledges the financial support provided by the Grant Agency of the Charles University (GAUK) under Grant No. 81108. Partial financial support from the Academy of Sciences of the Czech Republic under Grants Nos. ME08022 and KAN400720701 is also acknowledged.

## REFERENCES

1. R.Z. Valiev, R.K. Islamgaliev, and V. Alexandrov: *Prog. Mater. Sci.*, 2000, vol. 45, pp. 103–89.
2. *Investigations and Applications of Severe Plastic Deformation*, T.C. Lowe and R.Z. Valiev, eds., Kluwer, Dordrecht, The Netherlands, 2000.
3. B. Mingler, H.P. Karnthaler, M. Zehetbauer, and R.Z. Valiev: *Mater. Sci. Eng., A*, 2001, vols. A319–A321, pp. 242–45.
4. O.V. Mishin, D. Juul Jensen, and N. Hansen: *Mater. Sci. Eng., A*, 2003, vol. A342, pp. 320–28.
5. F.H. Dalla Torre, R. Lapovok, J. Sandlin, P.F. Thomson, C.H.J. Davies, and E.V. Pereloma: *Acta Mater.*, 2004, vol. 52, pp. 4819–32.
6. J. Lian, R.Z. Valiev, and B. Baudelet: *Acta Metall.*, 1995, vol. 43, pp. 4165–70.
7. Y. Estrin, R.J. Hellmig, and H.S. Kim: *J. Metastable Nanocryst. Mater.*, 2003, vol. 17, pp. 29–36.
8. C. Xu, M. Furukawa, Z. Horita, and T.G. Langdon: *J. Alloys Compd.*, 2004, vol. 378, pp. 27–34.
9. K.S. Siow, A.A.O. Tay, and P. Oruganti: *Mater. Sci. Technol.*, 2004, vol. 20, pp. 285–94.
10. P.G. Sanders, J.A. Eastman, and J.R. Weertman: *Acta Mater.*, 1997, vol. 45, pp. 4019–25.
11. S.R. Agnew and J.R. Weertman: *Mater. Sci. Eng., A*, 1998, vol. A244, pp. 145–53.
12. P.G. Sanders, M. Rittner, E. Kiedaish, J.R. Weertman, H. Kung, and Y.C. Lu: *Nanostruct. Mater.*, 1997, vol. 9, pp. 433–40.
13. Y. Estrin, L.S. Tóth, A. Molnari, and Y. Bréchet: *Acta Mater.*, 1998, vol. 46, pp. 5509–22.
14. S.C. Baik, Y. Estrin, H.S. Kim, and R.J. Hellmig: *Mater. Sci. Eng., A*, 2003, vol. A351, pp. 86–97.
15. K.T. Aust, U. Erb, and G. Palumbo: *Mater. Sci. Eng., A*, 1994, vol. A176, pp. 329–34.
16. N.Q. Chinh, J. Gubicza, and T.G. Langdon: *J. Mater. Sci.*, 2007, vol. 42, pp. 1594–1605.
17. F.H. Dalla Torre, A.Z. Gazder, E.V. Pereloma, and C.H.J. Davis: *J. Mater. Sci.*, 2007, vol. 42, pp. 1622–37.
18. J. Čížek, I. Procházka, R. Kužel, and R.K. Islamgaliev: *Monatsh. Chem.*, 2002, vol., pp. 873–87.
19. M. Janeček, B. Hadzima, R.J. Hellmig, and Y. Estrin: *Metallic Mater.*, 2005, vol. 43A, pp. 258–71.
20. P. Hautiojärvi and C. Corbel: in *Proc. Int. School Phys.: Enrico Fermi*, A. Dupasquier and A.P. Mills, eds., course CXXV, IOS Press, Varena, Italy, 1995, p. 491.
21. F. Bečvář, J. Čížek, and L. Lešták: *Nucl. Instrum. Methods A.*, 2000, vol. 443, pp. 557–77.
22. I. Procházka, I. Novotný, and F. Bečvář: *Mater. Sci. Forum*, 1997, vols. 255–257, pp. 772–74.
23. Z. Matěj, L. Nichtová, and R. Kužel: *Mater. Struct.*, 2008, vol. 15, pp. 46–49, open access: <http://www.xray.cz/ms>.
24. M.H. Shih, C.Y. Yu, P.W. Kao, and C.P. Chang: *Scripta Mater.*, 2001, vol. 45, pp. 793–99.
25. Y.M. Wang and E. Ma: *Appl. Phys. Lett.*, 2003, vol. 83, pp. 3165–67.
26. D.A. Hughes and N. Hansen: *Acta Mater.*, 1997, vol. 45, pp. 3871–86.
27. O.V. Mishin, D. Juul Jensen, and N. Hansen: *Proc. 21st Riso Int. Symp. Mater. Sci.: Recrystallisation-Fundamental Aspects and Relations to Deformation Microstructure*, N. Hansen, D. Huang, and D. Juul Jensen, eds., National Laboratory, Roskilde, Denmark, 2000, pp. 445–49.
28. D.G. Brandon: *Acta Metall.*, 1966, vol. 14, pp. 1479–87.
29. J.K. Mackenzie: *Acta Metall.*, 1964, vol. 12, pp. 223–25.
30. M. Dopita, M. Janeček, D. Rafaja, J. Uhlíř, Z. Matěj, and R. Kužel: *Int. J. Mat. Res.*, 2009, vol. 100, p. 6, DOI: [10.3139/146.110111](https://doi.org/10.3139/146.110111).
31. C.X. Huang, K. Wang, S.D. Wu, Z.F. Zhang, G.Y. Li, and S.X. Li: 2006 *Acta Mater.* vol. 54, pp. 655–65.
32. X.Z. Liao, Y.H. Zhao, S.G. Srinivasan, Y.T. Zhh, R.Z. Valiev, and D.V. Gunderov: *Appl. Phys. Lett.*, 2004, vol. 84, p. 592, DOI: [10.1063/1644051](https://doi.org/10.1063/1644051).
33. J.W. Christian and S. Mahajan: *Prog. Mater. Sci.*, 1995, vol. 39, pp. 1–157.
34. E. El-Danaf, S.R. Kalidindi, and R.D. Doherty: *Metall. Mater. Trans. A*, 1999, vol. 30A, pp. 1223–33.
35. V. Randle: *Acta Mater.*, 2004, vol. 52, pp. 4067–81.
36. B. Barbiellini, M.J. Puska, T. Torsti, and R.M. Nieminen: *Phys. Rev. B*, 1994, vol. 51, pp. 7341–44.
37. T.A. McKee, S. Saimoto, A.T. Stewart, and M.J. Scott: *Can. J. Phys.*, 1974, vol. 52, pp. 759–65.
38. J. Čížek, I. Procházka, P. Vostrý, F. Chmelík, and R.K. Islamgaliev: *Acta Phys. Pol.*, A, 1999, vol. 95, pp. 487–92.
39. J. Čížek, I. Procházka, M. Cieslar, R. Kužel, J. Kuriplach, F. Chmelík, I. Stulikova, F. Bečvář, and O. Melikhova: *Phys. Rev. B*, 2002, vol. 65, p. 094106.
40. Program Difpatan: <http://krystal.karlov.mff.cuni.cz/priv/kuzel/difpatan/default.htm>.
41. Th.H. de Keijser, J.I. Langford, E.J. Mittemeijer, and A.B.P. Vogels: *J. Appl. Cryst.*, 1982, vol. 15, pp. 308–13.

42. Z. Matěj, R. Kužel, M. Dopita, M. Janeček, J. Čížek, and T. Brunátová: *Int. J. Mater. Sci.*, 2009, vol. 100, DOI: [10.3139/146.110112](https://doi.org/10.3139/146.110112).
43. M.A. Krivoglaz, O.V. Martynenko, and K.P. Ryaboshapka: *Fiz. Met. Metalloved.*, 1983, vol. 55, pp. 5–17.
44. R. Kužel: *Z. Kristallogr.*, 2007, vol. 222, pp. 136–49.
45. E. Wu, A. MacGray, and E. H. Kisi: *J. Appl. Cryst.*, 1998, vol. 31, pp. 356–62.
46. M. Leoni, T. Confente, and P. Scardi: *Z. Kristallogr.*, 2006, suppl. 23, pp. 249–54.
47. M. Leoni, J. Martinez-Garcia, and P. Scardi: *J. Appl. Crystallogr.*, 2007, vol. 40, pp. 719–24.
48. P. Scardi and M. Leoni: *J. Appl. Crystallogr.*, 2006, vol. 39, pp. 24–31.
49. L. Balogh, J. Gubicza, R.J. Hellmig, Y. Estrin, and T. Ungár: *Z. Kristallogr.*, 2006, suppl. 23, pp. 318–86.